Chapter 18
Low-Energy Electron Microscopy

Juan de la Figuera and Kevin F. McCarty

Abstract Low-energy electron microscopy (LEEM) images a beam of low-energy electrons that have been reflected from a sample. The technique characterizes the sample's surface in real-space with nanometer-scale lateral resolution. Through a variety of contrast mechanisms, different aspects of the surface can be imaged, including the distribution of different phases and the location of atomic steps. LEEM instrumentation can also acquire electron diffraction patterns from local regions of the surface. The ability to acquire images quickly during temperature changes, while depositing films and exposing materials to reactive gases makes LEEM extremely useful for studying dynamical processes on surfaces. New developments include aberration correction systems for improved spatial resolution and bright spin-polarized electron sources.

18.1 Introduction

Low-energy electron microscopy (LEEM [1–7]) is a technique uniquely suited to perform dynamical observations of surfaces with nanometer resolution under vacuum. Figure 18.1 schematically illustrates the technique. A parallel beam of electrons is deflected onto a sample by a prism optic (beam separator). The electrons decelerate as they approach the surface because of an electrical bias applied to the sample. Electrons backscattered from the surface are accelerated and deflected by the prism into an imaging column and finally onto an imaging detector. Apertures in the illumination and imaging columns control the size of the electron beam on the sample and the electrons that strike the detector, respectively.

In many aspects LEEM is analogous to transmission electron microscopy (TEM [8]), the standard bulk microscopy technique. For example, both techniques

J. de la Figuera (✉)
Instituto de Química-Física "Rocasolano", CSIC, Madrid, Spain 28006
e-mail: juan.delafiguera@iqfr.csic.es

K.F. McCarty
Sandia National Laboratories, Livermore, CA 94550, USA
e-mail: mccarty@sandia.gov

G. Bracco, B. Holst (eds.), *Surface Science Techniques*,
Springer Series in Surface Sciences 51, DOI 10.1007/978-3-642-34243-1_18,
© Springer-Verlag Berlin Heidelberg 2013

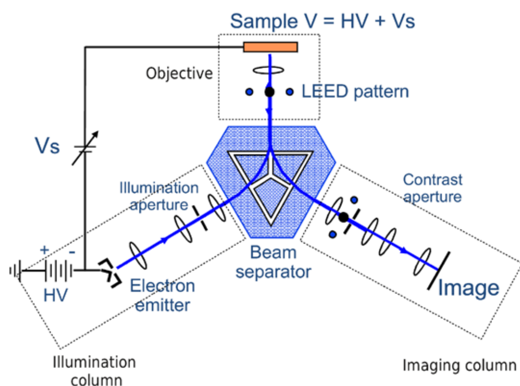

Fig. 18.1 Simplified LEEM schematic. Electrons from an emitter are formed into a parallel beam in the illumination column. After deflection by a prism optic, the beam impinges orthogonally onto a reasonably flat surface. The sample is biased to decelerate the electrons from their initial energy to a small energy, typically a few to tens of eV. Backscattered electrons are accelerated away from the sample and deflected in the opposite direction through the prism and into an imaging column. There a series of lens manipulates the electrons onto a two dimensional imaging detector. An illumination aperture defines the size of the electron beam on the sample, which is particularly useful for selected area electron diffraction. The contrast aperture in a diffraction plane selects the electrons that pass through to the detector

can acquire electron diffraction patterns from local sample areas and form images from the zeroth order electron beam (bright field imaging) or higher order diffraction beams (dark-field imaging). Although TEM can, and has been used to "look" at surfaces [9], it lacks strong contrast precisely because the operating conditions are optimized for bulk, not surface, observations. In particular, the high electron energy needed for the transmission mode gives low sensitivity to surface signals. A natural solution for observing surfaces is to employ low-energy electrons, which strongly interact with the surface. Since low-energy electrons won't penetrate through samples of practical thickness, the solution is to reflect the beam from the surface. This is the essence of LEEM. This idea was proposed before the development of "modern" surface science, with its heavy reliance on commercial technology to achieve ultrahigh vacuum (UHV). But due to technical challenges, only within the last two decades has the technique achieved its promise and become a versatile tool that allows the real *and* reciprocal space observation of surfaces during crystal growth, surface phase transitions or chemical reactions. This is achieved by using a variety of contrast mechanisms and imaging modes with nanometer-scale resolution, as explained in detail below (see Fig. 18.2). When coupled to a light source (be it a synchrotron, a laboratory-based laser or a helium discharge source) the instrumentation can provide most of the classical techniques for surface characterization: low-energy electron diffraction (LEED), scanning electron microscopy (SEM), X-ray photoelectron spectroscopy (XPS), ultraviolet photoelectron spectroscopy (UPS), etc. Use of spin-polarized electron sources or illuminated by polarized light add the capability to detect magnetic domains.

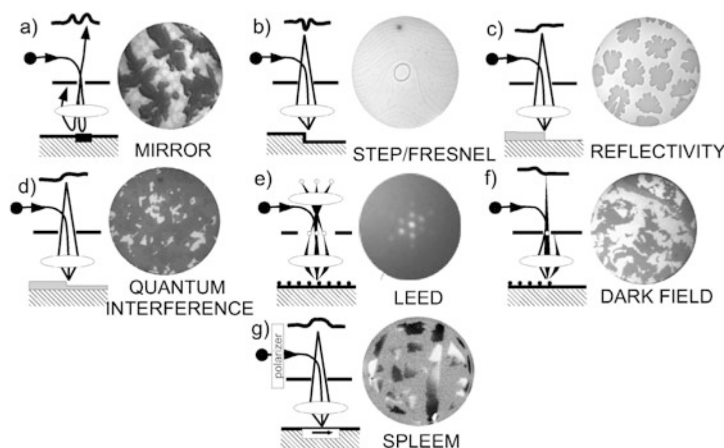

Fig. 18.2 Different working modes of a LEEM instrument. (**a**) Mirror electron microscopy of MgH_2 on Mg(0001), where the 1.25 eV electrons are reflected before striking the surface. The field of view (FOV) is 7 µm (reprinted with permission from [10]). (**b**) Phase contrast where atomic steps on a W(110) surface appear as dark lines because of interference in Fresnel diffraction (FOV is 10 µm). (**c**) Real-space image showing composition (diffraction) contrast between Cu islands and bare regions of a Ru(0001) substrate (FOV is 10 µm). (**d**) Phase contrast causing different thicknesses of Co on Ru(0001) to have different brightnesses. Average thickness is 7 ML (FOV is 10 µm). (**e**) LEED pattern of Cu/Ru(0001) showing 6-fold satellite spots around specular (zeroth order) beam. (**f**) Dark-field imaging mode using one of the satellite LEED spots in e) (FOV is 4 µm, from [11]). (**g**) Magnetic contrast in 2 ML thick islands of Co/Ru(0001) using a spin-polarized electron source, with a FOV of 4 µm. The schematics are adapted with permission from [1]

This chapter emphasizes what can and cannot be done with the current generation of LEEM instruments, with suggestions to make the most of them. We limit the scope to using electrons as the illumination source, i.e., pure LEEM. Please note, though, that all LEEMs can also perform photoemission electron microscopy (PEEM) if the appropriate light source is available [12].[1] LEEM can be used to analyze samples prepared ex-situ, as commonly done in synchrotron-based PEEM analysis. However, we particularly note that the real power of LEEM is being able to prepare materials under the carefully controlled conditions possible in an UHV-based instrument and track in real time the material's evolution. The ability to image quickly while changing temperature, annealing, exposing to gases or growing films allows for the rapid exploration of material systems. This productivity has led to a generation of LEEM users, as opposed to the LEEM "builders" of the pioneering

[1]In fact PEEM is more forgiving in terms of the samples that can be analyzed—some electrons are photoemitted normal to the surface plane even from very rough surfaces or from surfaces whose facets are not in the surface plane. In contrast, LEEM works best on relatively flat surfaces whose facets lie mainly within the surface plane. (For surfaces whose facets are not orthogonal to the electron beam, the specularly reflected electron beam is not transmitted through the imaging column under normal conditions.)

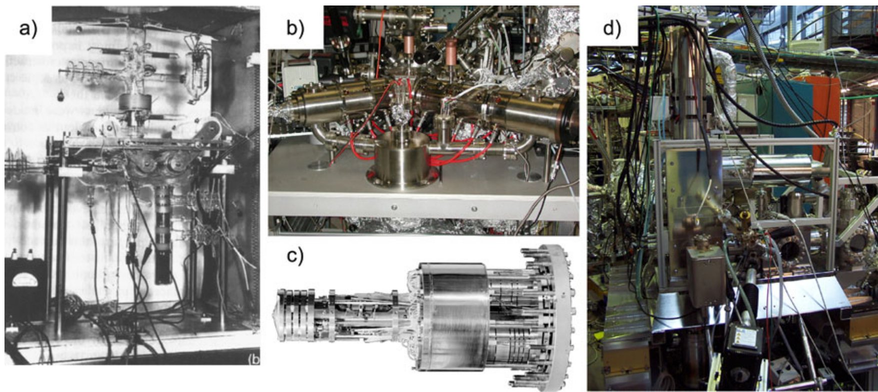

Fig. 18.3 (**a**) Glass LEEM test system, reproduced with permission from [13]. (**b**) Elmitec III instrument at Sandia National Laboratories, California. (**c**) Flange-on SPLEEM at Berkeley National Laboratories, California. (**d**) First Specs aberration-corrected LEEM/PEEM [18] at the BESSY synchrotron, Berlin

era [13]. The audience of this chapter are researchers interested in the LEEM capabilities. Hopefully some will turn into LEEM users.

Historical Development The LEEM concept, to use reflected electrons for surface crystallography, was proposed and developed by Ernst Bauer over a multi-decade period of time. The first feasibility tests where conducted in the 1960s with the construction of a glass system (Fig. 18.3a) [13]. The first functioning instruments providing quality images are from the mid-1980s [14]. In contrast, the last decade of the XX century can be considered the awakening age of LEEM. The first spin polarized instrument was constructed in the beginning of the decade (see Fig. 18.3c, [15]). The founding of the first successful LEEM company (Elmitec [16]) took place in 1995. The first work on employing aberration correction also started in the same decade, with the development of the SMART LEEM [17].

Developments have recently accelerated and the technique has attracted more attention [7]. By the end of the first decade of the XXI century, we have already two commercial companies (Specs [19] entering the field in 2009 to join Elmitec [16]) with different designs (see Fig. 18.3b and d). Both offer instruments with aberration correction optics, electron energy analyzers and resolutions that go below the 10 nm mark and approach the nm level. New developments are under way, such as a cryogenic LEEM using helium cooling and an aberration-corrected instrument with a spin-polarized electron source.

18.2 Background

Using reflected electrons to image a surface is a simple idea. But it raises the obvious questions of whether a surface would have enough electron reflectivity to allow for

an imaging technique, what mechanisms would provide contrast and what would be the achievable resolution [3, 13].

Imaging with Backscattered Electrons A large flux of electrons are needed to image a surface with reflected electrons in a non-scanning mode. The experience from low-energy electron diffraction (LEED) from single crystal surfaces indicated that a few percent of incident electrons should be backscattered at select energies [20]. Nevertheless LEED experience can be misleading since the technique traditionally uses electron energies above 50 eV due to experimental limitations [21]. But LEEM instruments work well at lower electron energies, where most of the contrast effects are strongest.

If the sample is at a voltage slightly more negative than that of the electron source, the entire electron beam is reflected just above the specimen surface. In this imaging mode, mirror electron microscopy (MEM [22]), the slow moving electrons are sensitive to the spatial and temporal variations in the electric field. In MEM there is obviously no scarcity of electrons for imaging. As those electrons do not actually reach the sample and they are very sensitive to changes in the electric field, their interpretation is not straightforward [23] but it can be used to reduce damage from the electron beam [10]. But even at higher energies, the reflectivity of a crystalline substrate is very high. Figure 18.4a shows experimental reflectivity, i.e., the reflected intensity normalized to the incident intensity, obtained from LEEM images as a function of electron energy. The reflected ratio of electrons is still very high (up to 20 %) at electron energies above the vacuum level, i.e., where the reflectivity falls below unity. This high reflectivity at low energies was theoretically predicted early on [3, 13], fueling the development of LEEM.

Contrast Modes The interaction of low-energy electrons with a substrate can give rise to a variety of contrast mechanisms. We have already presented the mirror mode (Fig. 18.2a), where contrast arises from differences in the electric field at the surface of the sample. Other contrast mechanisms also allow imaging: (1) the spatial distribution of different phases (Fig. 18.2c), (2) the thickness in atomic layers of films on a substrate (Fig. 18.2d), (3) the location of atomic steps on crystalline surfaces (Fig. 18.2b), and (4) the spatial distribution of differently oriented magnetic domains (Fig. 18.2g). The detailed reflected electron intensity at higher energies depends, among other factors, on the band structure of the substrate. To understand the relation of reflectivity and band structure it is instructive to consider the electron reflection under the single scattering approximation [28]. In such case, the reflected intensity would be directly related to the unoccupied band structure of the surface: a high reflectivity would occur when the density of available unoccupied electron states is low, and vice versa. Of course, multiple scattering is very important at LEEM energies, so it has to be taken into account using similar formalisms to those employed in LEED [28]. But even in the absence of detailed understanding of a particular system, it is expected that the band structure, and thus the electron reflectivity, from different materials should differ. In consequence, an energy-dependent contrast should arise from composition differences (see Fig. 18.4a). Whether two

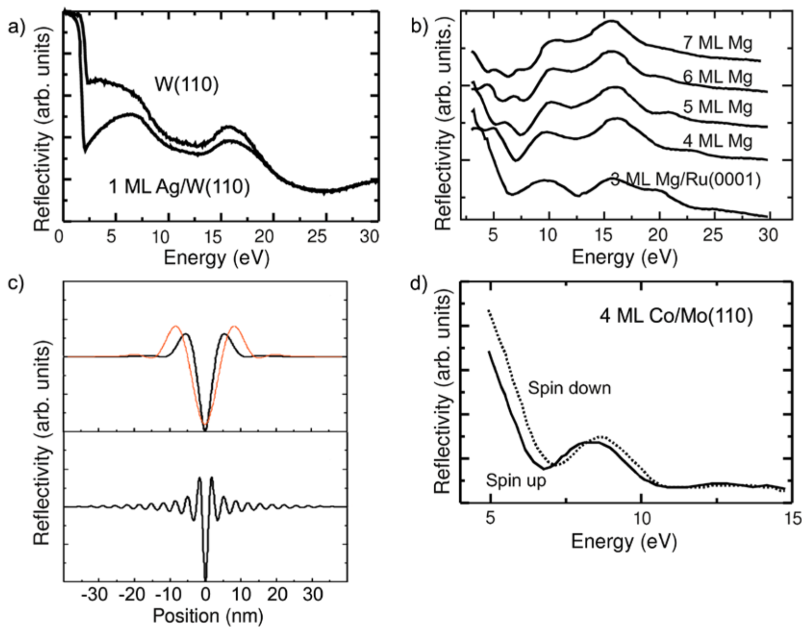

Fig. 18.4 Origin of image contrast in LEEM. (**a**) Electron reflectivity vs incoming electron energy for W(110), with and without a layer of Ag on top (reprinted with permission from [24]); (**b**) electron reflectivity as a function of film thickness for films of different thickness on Ru(0001), reprinted with permission from [25]; (**c**) real-space profile expected from Fresnel diffraction across a step with different aberrations, reprinted with permission from [26]; (**d**) electron reflectivity as a function of the incoming electron beam spin orientation relative to the sample magnetization in a 4 ML Co film on Mo(110), reprinted with permission from [27]

different elemental compositions give a useful contrast must be determined experimentally.

Another common origin of contrast in LEEM instruments is electron interference effects (phase contrast). For example, if a thin film has a sharp interface with its substrate, interference can occur between electrons reflected from the film/substrate interface and from the film surface. This gives rise to a Fabry-Perot effect that makes the electron intensity change as a function of electron energy and film thickness. Clearly, these changes in reflectivity can be used to detect film areas of different thickness, as shown for Mg films in Fig. 18.4b. Choosing appropriate electron energies allows imaging the formation of new film layers during layer-by-layer growth.

A similar effect allows detecting atomic steps: Fresnel diffraction [26, 29, 30] from electrons reflected at the lower and upper terraces around a substrate step gives rise to an oscillatory pattern of the reflected intensity around the step location (Fig. 18.4c, bottom). In non-aberration corrected instruments, the aberrations mask the fine detail of the Fresnel diffraction pattern so a step is typically seen as a single line (Fig. 18.4c, top). By observing the changes with focus and electron wavelength (i.e., energy) the up-down or down-up sense of the step can be determined [29].

In aberration corrected instruments, the fringe pattern around step edges has been observed [31]. Steps in LEEM have been detected on metal, semiconductor, nitride and oxide surfaces, and the easy observation of steps remains a crucial advantage of LEEM over other surface-sensitive electron microscopies.

Diffraction is another source of image contrast in LEEM. To improve contrast, LEEM images are usually acquired using a "contrast" aperture, which limits the diffracted beams that contribute to the observed image to the specular beam. This corresponds to the bright-field imaging mode in TEM [8]. By using deflectors in the beam separator, the illuminating or reflected beam can be tilted so real-space images can be formed from other diffraction beams (see Fig. 18.2f). If the surface has domains that give different diffraction patterns, each domain can be imaged in turn by selecting diffraction spots unique to each corresponding diffraction pattern (see Fig. 18.2f), i.e., by dark-field imaging.

18.2.1 Magnetic Contrast

Magnetic contrast can be obtained using electrons due to interactions of the illuminating electron beam either with (1) the magnetic field outside a ferromagnetic sample through the Lorentz force, or (2) by a direct interaction with the spin of the sample's electrons. In the latter case, exchange scattering or spin-orbit interactions can produce a dependence of the reflected intensity on the electron beam spin direction, and thus, provide magnetic contrast related to the magnetization of the sample, as shown in Fig. 18.4d. Either the source can be spin polarized or the spin polarization of the electrons can be analyzed after interaction with the sample.

The first method (Lorentz force) is implemented in LEEM by tilting the illumination beam and using incident electron energies close to mirror mode. Stripe domain patterns in a perpendicular magnetized film [32] and more recently bit patterns in magnetic recording media have been imaged [33]. But the most common method is to use a spin-polarized electron source (spin-polarized LEEM, or SPLEEM [34, 35]), where exchange scattering at the sample provides a contrast that depends on the scalar product of the spin direction and the sample magnetization. The magnetic contrast can be as high as 20 % of the topographic contrast for selected substrates or films, although it is often much smaller. To remove non-magnetic contrast from the images, it is common to acquire LEEM images with opposite illuminating electron-beam spin polarizations, denoted as I_+, I_-. Then the asymmetry ratio A, corrected by the electron beam spin polarization P, is calculated pixel by pixel:

$$A = \frac{1}{P} \frac{I_+ - I_-}{I_+ + I_-}$$

By selecting the spin direction in each of three orthogonal directions, the local magnetization direction can be determined with nanometer resolution.

Dark-field imaging is also usable for magnetic imaging in antiferromagnetic domains, even without a spin polarized incident beam. An antiferromagnetic structure

gives rise to a magnetic unit cell that is larger than the material's structural unit cell. Thus, it gives additionally diffracted beams of pure magnetic origin [36]. Using the magnetic diffracted beams as a source of dark-field contrast allows imaging antiferromagnetic domains in real-space. This method has recently been used on NiO [37]. The advantage of using spin-polarized electrons would be to determine additionally the spin-direction of the antiferromagnetic structure while also easily verifying the magnetic origin of the observed contrast.

18.2.2 Resolution

In contrast to TEMs where the actual resolution is orders of magnitude larger than the electron wavelength, in LEEM the experimental resolution is not far from this limit. The achieved resolution of an electron optics system can be written in a simplified description as the quadratic addition of several terms, the most important ones being the diffraction limit, the chromatic aberration and the spherical aberration. The latter two correspond to the same aberrations in light optics: considering a lens with a given focus length, spherical aberration arises because the focus depends on the radial distance to the center of the lens, while chromatic aberration corresponds to the dependence of the focal length on wavelength, i.e., electron energy [38]. Nearly all of the aberrations of a LEEM instrument arise in the objective lens [2, 38, 39], and unlike in TEM [8], a substantial part arises from chromatic aberration. Spherical aberrations are typically minimized using a contrast aperture centered around the specular beam. (A contrast aperture in PEEM also improves spatial resolution but reduces the signal available for imaging.) The chromatic aberration in LEEM is reduced by decreasing the energy spread of the electron source. For example, the current generation of instruments reaches 10 nm resolution with thermionic emission electron sources and 4 nm resolution with field emission sources, with aberration coefficients for chromatic aberrations of ≈ 150 m and for spherical aberrations of ≈ 0.5 m (at the image side) [39, 40].

The resolution of a LEEM is improved if the aberrations are reduced. But unlike in light optics, aberration correction in electron optics is quite recent. In LEEM instruments, the correction is performed by electron mirrors. Current instruments can remove the first order chromatic and spherical aberration and achieve 2 nm lateral resolution [18, 31]. Further improvements are anticipated.

18.3 Experimental Setup and Methods

From the technical point of view, a LEEM has much in common with a traditional TEM. Both use a series of lenses for manipulating the electrons that illuminate the sample and those that have interacted with the sample. Also, both form real-space images or diffraction patterns of the electrons that have interacted with the sample.

But LEEM works in reflection mode instead of in transmission, and at very low energies. Currently there are two successful commercial instrument designs [16, 19], plus a few unique, researcher-built systems.

A LEEM system (Fig. 18.1) consists of an illumination system, a beam separator, an objective lens system, and an imaging column. Additional lenses allow imaging the diffraction plane (back-focal plane) of the objective lens, while apertures can limit the illuminated area on the sample (i.e., the imaged area) and the angular spread in reciprocal space of the imaged electrons. While lenses and apertures are well-known elements of other electron microscopes (SEMs and TEMs), the beam separator is unique to LEEM. The objective lens is shared with other types of emission microscopes.

Lens System and General Considerations At the heart of any LEEM there are several electrostatic and magnetic lenses [43]. Electron lenses are well-developed and used in a variety of charged-particle instrumentation. The preference of electrostatic [44] vs magnetostatic lenses is mostly a question of convenience. While magnetic lens have smaller in aberrations, they are usually more bulky and difficult to cool down unless the coils are outside vacuum. They also rotate the electron spin and the image they form, although this effect can be avoided using self-canceling doublets.

Within the LEEM instrument the electrons have energies in the range of 10–20 keV. The objective lens decelerates the electrons to a few eV close to the sample. Decelerating the electrons requires either that the electrons travel at a high positive potential relative to the laboratory electrical ground, with the electron source grounded and the sample at a few eV, or that the electrons travel close to electrical ground and the electron gun and sample are at 10–20 kV negative potential. Obviously, having the sample close to ground potential is convenient from the experimental point of view. But it is not compatible with magnetic lenses, which have their central tube section at ground. Electrostatic lenses do not have this limitation.

The most popular commercial designs (see Fig. 18.5a, c) are dedicated LEEM instruments that employ magnetic lenses and have the electron source and sample at high voltage. In these instruments the illuminating and imaging sections and the objective and sample sections are housed in separate (but connected) vacuum chambers. The magnetic coils surround lengths of thin vacuum tubing at ground potential. As the connection between the sample area and the columns is through a small opening (several mm), differentially pumping permits imaging under pressures in the 10^{-4} mbar range while keeping the detector and electron emitter at UHV.

There are also fully electrostatic instruments (with the exception of the beam separator, see Fig. 18.5b) that have the electron source at ground and the sample close to ground. The use of electrostatic lenses makes for compact instruments that can be mounted on a standard flange (e.g., a 6″ CF flange) of a UHV chamber. Such systems comprise one commercial design (Elmitec IV [16]) and a few research systems [42, 45]. As all the electrostatic lenses are in the sample vacuum chamber, this type of LEEM usually is more demanding in terms of background pressure.

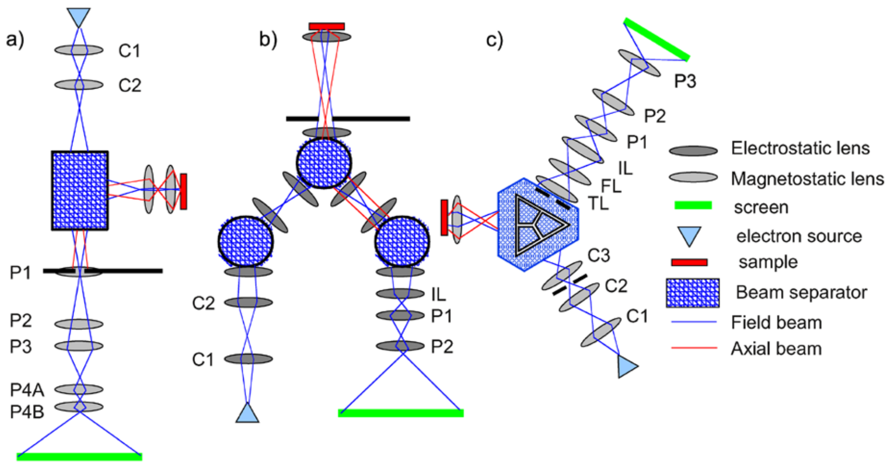

Fig. 18.5 (**a**) Specs/IBM LEEM design, reproduced with permission from [41]. (**b**) SPLEEM on-a-flange design, reproduced with permission from [42]. (**c**) Elmitec III design [16]

Illumination Sources and Condenser Optics Three types of electron sources are used in current LEEM instruments: thermionic, field emission and photoemission sources. The most popular thermionic source is based on a LaB_6 single crystal emitter. It is inexpensive, has a long lifetime, and is quite sturdy in UHV environments [46]. The main limitations is the energy spread of about 0.6 eV and the brightness.

More recently, cold field emission (CFE) sources are gaining in popularity. Although the LEEM market is too small to fuel electron source development, the TEM and SEM markets have provided for easy-to-use and reliable sources. The energy spread for cold field emission is $\sim$0.25 eV, significantly improving resolution.

Finally, GaAs sources are the only spin-polarized electron sources presently used for magnetic imaging (i.e., SPLEEM), both in commercial systems [16] and in custom-built instruments [15]. The energy spread is even smaller than cold field emission sources (0.11 eV). A GaAs electron source [47] consists of a GaAs cathode conditioned to negative electron affinity (NEA), which emits electrons when illuminated by circularly polarized light from a diode laser. Driving the GaAs cathode to NEA condition requires an appropriate coverage of cesium and oxygen. The need to properly prepare the GaAs surface (cleaning it, and then depositing Cs and oxygen) together with the requirement of extreme vacuum (well below 10^{-10} mbar) for reasonable lifetimes of the prepared cathode make this electron source quite demanding.[2] The traditional design suffers from the large size of the illuminating laser beam, which consequently provides a brightness lower by about 10^3 $A \times cm^{-2}$ sr^{-1} than a thermionic LaB_6 source. Recent designs focus the laser beam to a micrometer area and provide brightness comparable with thermal sources [48]. The spin

[2]If properly tuned, cathode preparation is routine and lifetimes are several days.

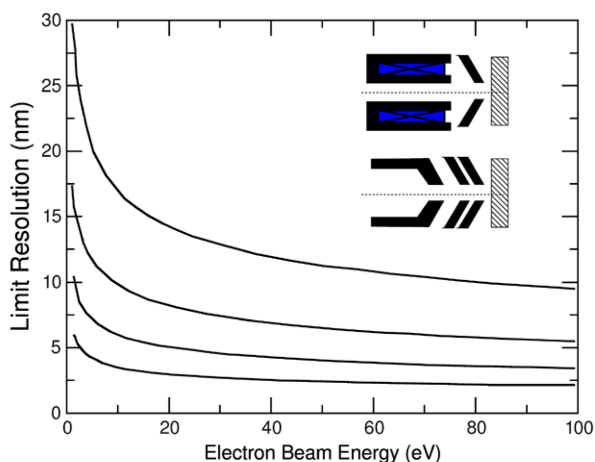

Fig. 18.6 Resolution limit as a function of the electron beam energy at the sample for a given energy spread (ΔE) and acceleration voltage (E), adapted with permission from [39]. The curves shown the resolution from top to bottom for $\Delta E = 2$ eV and $E = 5$ kV, $\Delta E = 2$ eV and $E = 15$ kV, $\Delta E = 0.25$ eV and $E = 5$ kV, $\Delta E = 0.25$ eV and $E = 15$ kV respectively. The *inset* shows two popular objective configurations adapted with permission from [50]: a fully electrostatic tetrode (*lower schematic*) and an electrostatic acceleration electrode paired with a floating magnetic lens (*upper schematic*)

direction of the electrons is perpendicular to the GaAs cathode. A spin manipulator between the GaAs cathode and the condenser optics is used to turn the spin direction to any desired orientation relative to the sample [40, 49].

The condenser lenses are used to obtain a parallel beam of electrons before reaching the sample by providing a demagnified image of the source at the objective back-focal plane. Having several condenser lenses provides maximum flexibility, although some recent designs use a minimalist approach of a single condenser lens [19]. Additionally the illuminating system can contain some deflectors and/or astigmatic octupole correctors. Typically the illuminated area on the sample is 10–100 μm in diameter depending on the design and source. Apertures can reduce the area down to about 0.2 μm.

Objective The objective lens performs a dual role: for the incoming electron beam its functions are to slow the beam from 10–20 keV to the eV range and provide a parallel beam of electrons at the sample by collecting the electrons at its back-focal plane. For the electron beam reflected from the sample, the objective increases the beam energy from several eV to 10–20 keV and forms a magnified real image of the emitted electrons (typical magnifications range from 10–50×). A diffraction pattern exists at its back-focal plane. All objectives are thus composed of an accelerating lens and an additional electrostatic or magnetostatic lens for focusing (see the inset in Fig. 18.6). As shown in Fig. 18.6, the two most important factors for determining the resolution in a LEEM objective are (1) the acceleration voltage, or conversely, the field strength between the sample and the first lens, and (2) the energy spread of

the electrons. In all current instruments, the field strength is about 10–20 keV/mm.[3] Several objective designs have been tried (see inset of Fig. 18.6) with an electrostatic tetrode or a magnetic lens behind the accelerating lens being the most popular (the latter has smaller aberrations [50]). Nearly all the spherical and chromatic aberrations that limit the final instrument resolution originate at this objective system. The quantification of the objective aberrations has been studied in detail [39] due to the current interest in the aberration correction of LEEM instruments.

Beam Separator The function of the beam separator is to separate the electrons going into the sample from the electrons leaving the sample. In its simplest form it consists of a square or circular magnetic dipole with two parallel pole plates excited by a coil. A limitation of this design is that a dipole field focuses the electrons that move in a plane normal to the magnetic field. This means that the focusing properties are very different in the two axis of the electron beam. A solution to this problem is to add extra lenses for the focusing function, as in the Berkeley SPLEEM [15] (Fig. 18.5b), which uses double dipoles with opposite magnetic fields in both the illuminating beam and in the imaging section together with additional electrostatic lenses in the beam separator.[4] Most of the current systems are based on a 60° deflector that uses an array of dipole fields [51] (see Fig. 18.5c). However, 90° deflectors are being increasingly used [41] (see Fig. 18.5a). They allow stacking the optics vertically, a particular advantage for aberration correction, where an additional beam separator is needed [18]. They are constructed from a central (square) dipole magnet, surrounded by one [41] or more rings [33] at different magnetic potentials, or by additional round electrostatic lenses [52].

Imaging Optics and Imaging Systems The imaging column contains several lenses arranged so a field of view between about 1–100 μm can be imaged. After the last imaging lens, the electron current is amplified by microchannel plates before impinging on a phosphor screen. A digital camera outside of the vacuum chamber records images of the screen.

The channel-plate-based detectors are delicate and typically do not have a uniform response across their area. The main operational danger of a LEEM lies in the microchannel plates: excessive electron flux can damage the plates and the phosphor, giving rise to dead areas in the detector. Moreover, runaway events in the detector can cause damage even when no electron beam is present. When switching from real-space mode to a diffraction pattern, care has to be exercised not to exceed the maximum current of the channel plates. Controlling the image intensity safely is essential for the current detectors. In some instruments, the preferred way to control intensity is changing the illuminating beam current, while other instruments change

[3]One fact in LEEM that is often overlooked is that the sample always experiences such an applied field. As the resolution degrades mildly with acceleration voltage [39] (see Fig. 18.6), the electrical field might be somewhat reduced for delicate samples.

[4]The opposite magnetic fields cancel the spin rotation of an individual dipole so that an electron transiting the complete beam separator does not change spin direction.

the channel plate voltage. Direct imaging sensors without channel plates are being tested but they have smaller active areas and cannot be baked at the temperatures typically used to achieve UHV conditions [53].

Energy Filters Additional capability comes from the ability to filter the electrons emitted from the surface by their energy. In its simplest form, LEEM makes images from elastically reflected electrons. Any inelastically emitted electrons are then an unwanted background in the images and in LEED patterns. But the inelastic electrons also contain information, as do electrons in photoemission. An energy filter extracts information from these electrons.

Two types of energy filters are being used. One type decelerates and then bends the electron beam, which disperses it by energy. A recent design takes advantage of the energy dispersion within the beam separator itself to provide energy discrimination without extra optical elements other than apertures [41]. The magnetic field of the beam separator gives a chromatic dispersion of about 5 μm/eV [54], useable but much smaller than that of the first type of filter [1].

Two modes of operation are common. In the first, the dispersive plane of the energy filter is imaged onto the detector. Converting image intensity versus position into a count rate vs. energy gives a traditional spectrum. An aperture in the beam separator is used to select the analysis region on the sample, analogous to selected-area LEED. In the second mode, an aperture in the dispersive plane is used to select a given energy bandpass. The passed electrons are then formed into an energy filtered image. Changing the sample potential changes the electron energy that passes through the filter's aperture to the detector.

In a pure LEEM instrument (no light source), a filter enables electron energy loss spectroscopy (EELS) [55, 56] and Auger spectroscopy. Setting the filter energy to a given loss or Auger peak gives spatial maps of phase or elemental composition. When combined with light sources, the energy filter allows photoemission spectroscopy and microscopy, as is most powerfully practiced at synchrotrons. However, intense He discharge lamps and ultraviolet lasers are enabling photoemission spectromicroscopy in laboratory environments [57].

Aberration Correction Systems As mentioned before, simple electrostatic or magnetostatic lenses always have the same sign of spherical and chromatic aberrations. To increase the resolution and the acceptance angle (throughput) of the instrument, the first order aberrations have to be corrected. A successful approach is through the use of electron mirrors [38], which have opposite chromatic and spherical aberrations than lenses. Such an electron mirror can be realized with a regular electrostatic lens but with a much higher voltage, so the incoming electrons are reflected back. The main drawback of using an electron mirror is that the electrons going towards the mirror and the electrons reflected have to be separated. This means that electron mirrors had to wait until the development and familiarity with beam separators, which are specific to LEEM. With the present beam separator expertise, the adoption of electron mirrors for aberration correction is finally taking place. The current designs use either a special four-way beam separator, or stacked beams separators of the 60° [16, 40] or 90° type [18].

Methods to measure the aberrations and adjust the mirror voltages to correct for the first order aberrations all while changing other instrument parameters such as the electron energy are under development [31, 39].

18.4 Applications

LEEM instruments have been applied to a variety of surface science phenomena. Here we highlight some applications where LEEM instruments have added new insights. Most LEEM experiments share the same profile: first an atomically clean surface must be obtained, so either sputtering or annealing cycles are performed. Already at the cleaning stage, the surface state should be checked often (or continuously if possible) in LEEM. The full power is realized when all processes such as exposure to molecular or atomic fluxes are done under LEEM observation. Unless preparation procedures are very cumbersome, several experimental runs can be performed per day. This allows for rapid exploration of the experimental parameter space. LEEM instruments have been used to study metals, semiconductors or compounds such as oxides or nitrides. In most areas, the breath of the experiments has been limited more by instrument availability rather than by the technique itself.

18.4.1 Observation of Clean Surfaces

The high-resolution observation of metal and semiconductor surfaces [14], locating the atomic surface steps, was a hallmark in LEEM evolution. As mentioned before, atomic steps are imaged by Fresnel diffraction. Although the bulk of the LEEM work has been performed on metal and semiconductor surfaces, more complex systems such as binary oxides [58–60], nitrides [61–63] and quasi-crystals [64, 65] have been explored (see Fig. 18.7a–d).

The surface morphology can be directly imaged by locating the atomic steps. As LEEM can select a field of view between a few microns to up to tens of microns, it is possible to explore large areas of a surface. This often provides a dual role. On one hand, some particular types of surface areas can be located, either large flat terraces, step bunches or features created by, for example, a focused ion beam (FIB) [66]. On the other hand, sampling can reveal the average state of the surface, information that can guide experiments using complimentary techniques. Easily exploring parts of the surface millimeters apart serves to avoid the common "tunnel view" of STM where a restricted area of the surface is assumed to be representative of the full surface.

Besides steps or dislocations, which themselves can give rise to steps [62], stacking faults and twins are defects that occur in films and surfaces. Both defect types are easily located in LEEM through a combination of dark-field and bright field imaging [11, 67, 68]. In the case of two structures related by twinning, the diffraction pattern of one twin is rotated by 180° from the other's pattern. Selecting a diffracted

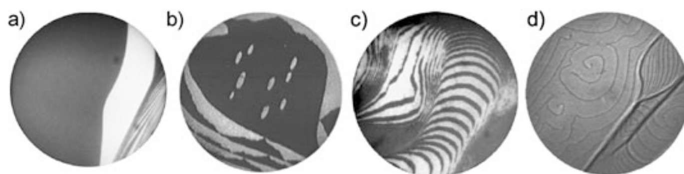

Fig. 18.7 LEEM images of different surfaces. (**a**) Dark-field image using an first order diffraction spot of Ru(0001), reproduced with permission from [69]. The field of view of 10 µm. (**b**) Dark-field image of Si(100) acquired with a diffraction spot from one of the domains of the 1×2 reconstruction, reproduced with permission from [71]. The field of view is 5.5 µm. (**c**) Bright field image of TiO_2(110) reprinted with permission from [58]. The field of view of 10 µm. Diffraction contrast causes the 1×2 reconstruction to be dark compared to the bulk-like 1×1 phase. (**d**) TiN(111), reprinted with permission from [63]. The field of view is 5.6 µm

spot in dark-field imaging from one twin will give the real-space distribution of that twin. Bright field imaging can be used to determine whether the dark-field image is a pure twin or a stacking fault. In the former case, no bright field contrast would be possible by symmetry. In the latter, the stacking fault can be considered a change in the unit cell of the last layers and would be seen in bright-field [68]. Sometimes the structure of the surface is such that crystallographically inequivalent but energetically equivalent terminations are possible. Examples include hcp [69] and wurzite [70] structures. In both structures the local sequence of layers in the direction perpendicular to the basal plane is such that consecutive atomic steps give rise to a rotation by 180° of the local environment, i.e., the crystal symmetry group has a screw symmetry operation. Then, a dark-field image from a first-order diffracted spot gives an image with alternatively white and dark terraces separated by atomic steps (see Fig. 18.7a).

18.4.2 Surface Dynamics: From Adatoms to Phase Transitions

The evolution of surfaces has an important role in nanoscience. Such evolution is determined by thermodynamic and kinetic effects. The ability of LEEM to locate steps in real time makes it a powerful technique for observing the evolution of surfaces under controlled conditions.

Steps As LEEM can easily image single-layer atomic steps, a popular focus has been step dynamics, both in semiconductors [72, 73] or metals [74, 75]. Although the emphasis has been on simple surfaces by extracting accurate properties for comparison with theory, an obvious evolution of the technique is to expand it to more complex surfaces such as quasi-crystals [65]. Through the interpretation of the step motion, both properties intrinsic to the steps (such as line tension) and adatom-step interactions can be determined.

A related line of work has been examining the evolution, not of more or less linear steps, but of closed steps forming islands or pits [76]. By measuring in detail

the evolution of a non-equilibrium structure, such as an island array on a substrate terrace or a mound of islands, the evolution towards equilibrium can be directly compared with model simulations incorporating the mass carriers and their interaction with steps. When a set of differently sized islands on a terrace undergoes Ostwald ripening, the dependence of the island line tension on curvature makes smaller islands decay and larger islands grow [71]. The particular way the islands area changes with time gives information about the limiting process that the mass carriers experience: either diffusion along the terraces or attachment/detachment from step edges. But also the role of bulk diffusion has been highlighted in experiments studying the evolution of Pt(111) [77]. In the more complicated case of NiAl(110), separating the effects of bulk vs surface diffusion [78] required taking advantage LEEM's ability to image while oscillating the sample temperature. Another option in LEEM is the ability to observe a surface at very high temperatures, needed for refractory metals such as Rh(001) [79]. Adsorbates can also be deposited in real time during island decay, helping solve long standing questions about the role of impurities in surface evolution. The influence of sulfur on Cu island decay has thus been explained in terms of the formation of S-Cu units that serve as additional and very efficient surface mass carriers [80]. A novel development is the ability to deposit ions while imaging. The adatom concentration can be enhanced or depleted, depending on the ion energy [81, 82]. In this way, the phase space under which surface evolution can be observed is greatly expanded.

Thermal Adatoms Thermal adatoms on a crystal surface equilibrate with sinks such as steps. The concentration and distribution of the adatoms can be deduced from the detailed time evolution of the steps. This information can also be determined by studying island nucleation [83]. But to determine directly the concentration of adatoms is complicated as thermal adatom concentrations are often very low, and the adatoms themselves can move large distances, precluding the use of STM-related techniques at any but the lowest temperatures, where the surface evolution is nearly frozen. LEEM can be used to determine both the concentration and distribution of thermal adatoms on a surface by monitoring changes in the surface reflectivity. Adatoms cause the incident beam to be scattered diffusely, reducing its reflected intensity. Therefore in a bright field image a decrease in intensity can be related to an increase of adatom concentration. The method has been applied to metal [24] and carbon adatoms [84], and the sensitivity easily reaches concentrations of 10^{-4} ML.

Phase Transitions LEEM's rapid imaging gives a powerful approach to observe surface phase transitions, which are typically driven by changing temperature [85]. Depending on the phases involved, different contrast mechanisms can be used in imaging. Unlike using reciprocal space techniques to probe phase transitions, a real space view of the surface allows determining whether there is phase coexistence. An early success of LEEM was the real time observation of the transition between the Si(111) 7×7 and 1×1 surface structures [86]. The detection of phase coexistence showed directly that the transition was first order. The subtleties of the 7×7–1×1

phase transition have been studied in detail by LEEM, shedding light on the role of bulk diffusion [87] and the extended temperature range of the phase coexistence [88]. The richness of the system has motivated recent studies on the impact of the phase transition on island decay [89].

Another classic surface phase transition is the roughing transition. Although not as spectacular as Si's 1×1 to 7×7 transition, the roughening transition of Si/Ge alloys has been characterized by LEEM [90]. Additional phase transitions have been studied on other semiconductors [91] or metal/semiconductor surfaces [92]. Phase transitions in metals and oxides have received much less attention [59]. It is a glaring omission that well-known metal reconstruction phase transitions have not yet been studied by LEEM.

18.4.3 Thin Film Growth: From Self-assembly to Film Dewetting

One field where a real-time view of a process is most rewarding is thin-film growth. There are a limited number of techniques that allow real-time monitoring of thin-film growth by molecular beam epitaxy (MBE), pulsed laser deposition (PLD) or reactive MBE. The most used technique is reflection high-energy electron diffraction (RHEED), which only provides reciprocal-space information averaged over a macroscopic area. Consider the growth mode of a film by step-flow, i.e., a growth mode in which the deposited material adds to at the preexisting steps and the film grows in strict layer-by-layer mode. Step-flow gives rise to films as flat as their substrate. But as no new steps are created on the growing film, RHEED is completely blind to the number of layers deposited. LEEM is the only general purpose surface science technique that allows real-time *and* real-space monitoring of the surface growth front in PLD and MBE. For example, in Fig. 18.8 we show two examples of thin-film layer-by-layer growth, either by step-flow (Fig. 18.8a) or by island nucleation (Fig. 18.8b). The capabilities of LEEM to explore growth have been used to monitor metal growth both on metals [25, 66, 68, 93–97] and semiconductors [98, 99], semiconductor growth [100, 101], graphene growth both on metal [84, 102–110] and on SiC [111–113], and oxide growth [114–120]. The particular role of dislocations in thin-film growth has been studied in semiconductors [121], metals [62, 67, 122], and nitrides [62].

The surface sensitivity of LEEM is usually stated to arise from the short inelastic mean free path of low-energy electrons. However, at typical imaging energies, the mean free paths can be surprisingly long. This implies that changing the focus allows the buried interface between the film and the substrate to be easily imaged [125]. As heating to high temperatures under observation in LEEM is straightforward, sublimation of thin films can be tracked [126]. At lower temperatures, the dewetting process by which a continuous film breaks up [127] or a thinner film roughens to form large 3-dimensional islands (mesas) has been studied in metals [128]. Thanks to LEEM observations, the latter process has been used as part of a method [129] to produce large flat areas in metallic crystals by sputtering a mesa-containing thin film [130].

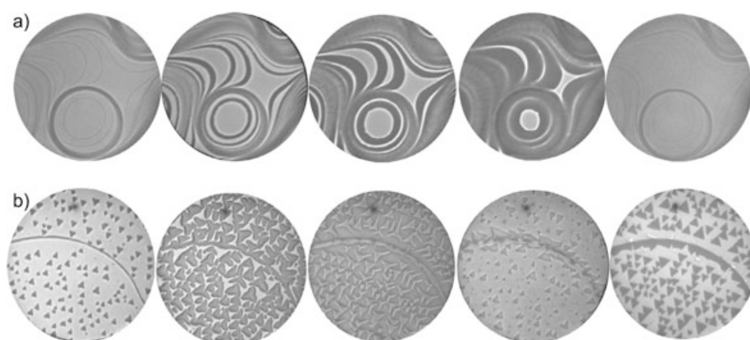

Fig. 18.8 Thin-film growth. (**a**) Step-flow in the growth of 1 ML Cr on W(110), adapted with permission from [123]. (**b**) Layer-by-layer island nucleation growth in the growth of the first three layers of Co on Ru(0001), adapted with permission from [124]. The field of view of each sequence is, respectively, 7 and 10 μm

Furthermore, the capabilities of LEEM allow not only for monitoring the growth front of the film, but for a detailed structural characterization of the film itself. By combining the different working modes of a LEEM, the interlayer spacings, the stacking sequence of the film layers or the presence of stacking faults can be resolved for each film thickness [25, 68, 94, 97].

In the same way as TEM characterizes the structure of a bulk film, LEEM can determine the microstructure of films a few atoms thick. As a complex example [11], Cu on Ru(0001) has a thickness dependent misfit dislocation network. For films two monolayers thick, the dislocation network consists of sets of parallel dislocations. Three equivalent rotational domains occur, with the dislocations aligned along the three equivalent directions of the substrate. Even if the dislocation spacing in the domains is below the resolution limit of a non-aberration corrected LEEM, each rotational domain can still be imaged in dark-field using its unique diffraction spots (see Fig. 18.9b, and composite image in Fig. 18.9c). But in addition to the rotational domains, there are also domains within the film that differ in their stacking sequence. This additional microstructure can be imaged in bright field using an appropriate energy (see Fig. 18.9d). In this way, the evolution and the interplay between the different types of film defects can be determined. In this particular example, it was found that the healing of stacking domains was impeded by the threading dislocations present at the boundaries of rotational domains.

Self-assembly of Submonolayer Films The quest for ordered arrays of nanoscale objects has popularized the study of self-organized patterns in submonolayer film growth. Monolayer-height islands deform the substrate, giving rise to an elastic interaction between islands. The competition between the (short-range) boundary cost of creating island edges is then compensated by the (long-range) elastic interaction between island edges. The resulting self-assembly gives rise to striped patterns on uniaxial systems, while isotropic systems should exhibit a transition between a bubble phase (round islands in an hexagonal pattern), a stripe phase and an

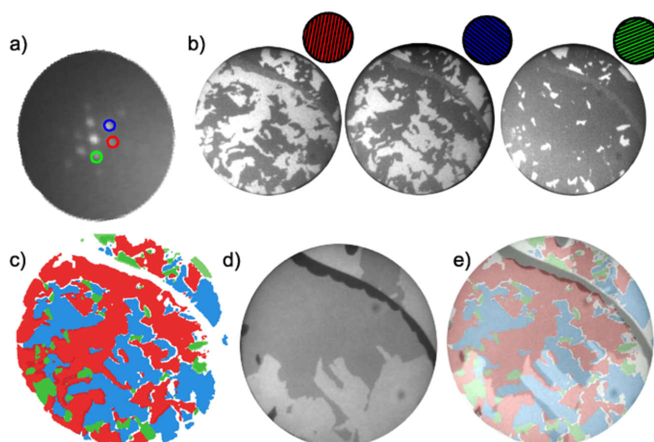

Fig. 18.9 Microstructure of a 2 ML Cu film on Ru(0001), adapted with permission from [11]. (**a**) LEED pattern arising from the superposition of three rotational domains. (**b**) LEEM dark-field images from three different diffraction spots. The *bright regions* map the spatial distribution of the three rotational orientations. (**c**) Composite image of the dark-field images in (**b**). (**d**) LEEM bright-field image showing the distribution of the two different stacking sequences (*light* and *medium gray*). (**e**) Complete microstructure of the film showing both rotational and stacking domains. The field of view is 5 μm

inverted bubble phase. The origin of the patterns lies thus in the thermodynamics of the system. They have been observed for metals [131–134] and semiconductors [135–137]. Pb islands on Cu(111) can be considered a model system for stress domain self-assembly [138–142]. Pb on Cu forms a disordered alloy until a critical Pb concentration is reached. Then, in addition to the disordered alloy, islands of pure Pb nucleate on the surface. As the coverage of Pb is increased, the shape of the Pb islands changes from round islands, to stripes, and then to inverted droplets, as predicted by theory and shown experimentally in Fig. 18.10. The pattern periodicity depends exponentially on the ratio of boundary cost (step energy) and elastic interaction. In the Pb/Cu system, detailed studies of the fluctuations of the stripe phase allowed an accurate and independent measure of the boundary energy. The long range elastic interaction was measured by studying fluctuations of the island positions in the droplet phase. The predicted periodicity matched the experimentally observed value.

Alloys Alloying in thin films or surfaces can be followed in LEEM. But as LEEM cannot image the atomic scale, quantifying the alloying is usually indirect. NiAl bulk alloys have been studied by following changes in the surface morphology [143, 144]. At surfaces, alloying and dealloying on refractory metals have been detected by the morphology of the surface [145] or more directly by the observation of a specific alloy-related LEED pattern [146, 147]. The effects on island growth and motion can be striking. In Sn on Cu(111) the formation of an alloy actually propelled the Sn islands across the substrate leaving a trail of surface alloy [148]. In

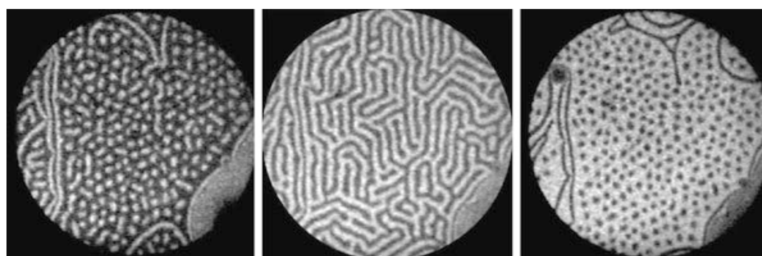

Fig. 18.10 Self-organization of Pb islands on Cu(111) as a function of the Pb coverage, reprinted with permission from [139]. The field of view is 1.8 μm

Pd/Ru(0001), at specific temperatures and deposition rates, the formation of a surface alloy around growing Pd islands impedes further island growth except at particular points. This produces distinctive labyrinthine-shaped islands, whose growth was followed in real time [96].

Magnetic Domain Studies We consider here imaging magnetic domains in ferromagnetic films or surfaces (studies of spin-dependent electron reflectivity are discussed in the VLEED section below). The number of SPLEEM instruments at the time of writing this chapter is just four, so the span of the different material combinations tested is extremely limited. Ferromagnetic elements that have been shown to provide usable contrast in SPLEEM include all the 3*d* magnetic transition metals (Fe, Co, Ni), and the rare earth Tb. In compound form, magnetite islands also give SPLEEM contrast [120]. Other compounds and alloys await experimental studies.

A straightforward SPLEEM application is to determine the magnetic domain structure of surfaces and islands [149–154]. In this way, finite-size effects on the magnetization patterns can be determined, such as the transition between single domain and vortex states in 3-dimensional magnetic islands [155], or the magnetization patterns in elongated islands [156, 157]. The Curie temperature is determined by measuring the temperature where magnetic contrast is lost. But the important point is that the Curie temperature can be measured locally, so it is easy to check the effect of thickness [124] or the local environment [158].

Since SPLEEM can measure each component of the magnetization, it can perform 3-dimensional magnetometry [159] by changing the spin-orientation of the illuminating electron beam in orthogonal directions. It then becomes a powerful method to explore spin-reorientation transitions [124, 152, 159–163]. For example, consider the magnetization of Co on Ru(0001). The growth can be interrupted at intermediate coverages between 1–2 ML and 2–3 ML, and the magnetization along two in-plane directions and the out-of-plane direction can be measured in sequence. As Fig. 18.11 shows, the 1 ML and 3 ML areas are only magnetized in-plane, unlike 2 ML areas, which are magnetized out-of-plane. Thus, there are consecutive spin-reorientation transitions as a function of thickness. Further studies followed in real time how the capping the Co with noble metals also produce additional

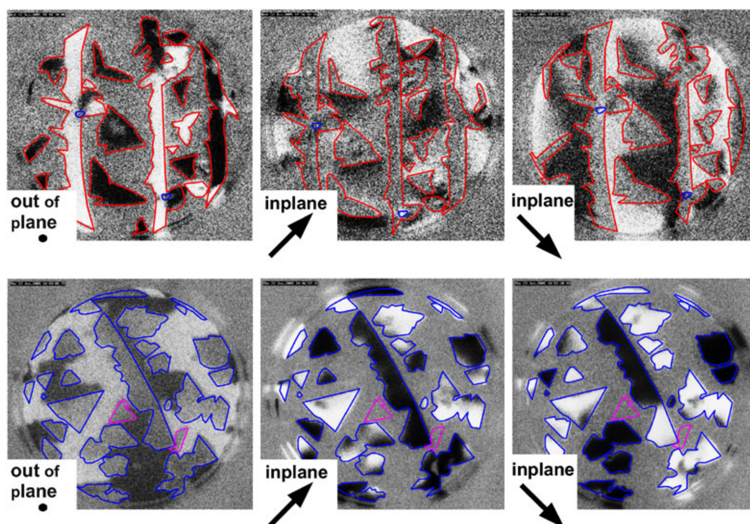

Fig. 18.11 3-D magnetometry in Co/Ru(0001) ultra-thin films, reproduced with permission from [124]. *Top row*: SPLEEM images of the same film with 2 ML Co thick islands on a continuous 1 ML Co layer. Each SPLEEM image shows magnetic contrast along the direction indicated in the *left-lower corner*. *Bottom row*: SPLEEM sequence acquired on a film with 3 ML Co thick islands on a continuous 2 ML Co layer. FOV is 2.8 μm

spin-reorientation transitions [162]. Another theme is the study of the coupling between magnetic layers. But unlike measuring magnetization using PEEM techniques, SPLEEM lacks chemical sensitivity, making the extraction of information about the magnetization of individual layers more involved.

18.4.4 Determining Surface Crystallography and Electronic Structure

Low-energy electron diffraction (LEED), the measurement of diffraction patterns with reflected electrons is the standard surface science crystallographic tool [21]. LEEM is an excellent technique to measure LEED. This can be done both in real space (with a contrast aperture, so only the specular beam is measured) or in reciprocal space and with spin-polarized electrons in SPLEEM instruments. We discuss separately the diffraction information of the "traditional" LEED energy range (50–400 eV) and that of VLEED (0–50 eV). The distinction serves to underline the different characteristics of the information obtained in each energy range.

"Traditional" LEED The "traditional" LEED allows determining surface structures comprising up to a hundred atoms with picometer accuracies by an iterative comparison of the intensity of diffracted beams vs electron energy with multiple

scattering calculations from a model structure [20, 28]. In the 50–400 eV energy range the electron mean free path is small (a few atomic layers), giving it extreme surface sensitivity. The energies are high enough that the band structure of the surface can be disregarded, with the calculations employing a muffin-tin approximation. In this range, the usual collection method in LEEM is to image the back-focal plane of the objective, i.e., the diffraction pattern of the electrons leaving the sample surface.

There are several experimental advantages to acquiring LEED data in LEEM. As the illumination and the reflected electrons paths are separated by a beam separator, there is no problem measuring the specular beam or its closely spaced satellites under normal incidence conditions. The sample manipulator and electron optics allow the incident beam to be aligned precisely normal to the surface. The optical (light) path from the sample is also separate from the electron path, so measurements can be performed even when the sample is hot. (In a regular LEED instrument, light from the hot sample or the heater apparatus gives a substantial background intensity on the detector screen, making measurements at elevated temperatures difficult.) As all LEEMs include high gain microchannel plates for imaging, they can acquire LEED patterns at very low electron beam intensities. The position of the diffracted spots on the detector does not change with incoming electron energy because the diffracted electrons are deflected during their acceleration away from the surface in a way that exactly cancels the change in initial emission angle with energy [3]. Thus, there is no need for sophisticated tracking of diffracted beams with energy while measuring their intensity. Furthermore, the ability to change the power of the lens in the imaging column means that a LEEM instrument can serve as a reasonable spot-profile analysis LEED system (SPA-LEED [164]). But the reason why LEED in LEEM stands apart is the ability to select the area from which the LEED information is obtained by using the real-space imaging mode of LEEM. First a region is characterized by real-space imaging. Then a particular region is selected for LEED analysis. Diffraction from regions of interest as small as $\frac{1}{4}$ μm in diameter can be routinely obtained.

Nevertheless there are some limitations acquiring LEED in LEEM. One is that the size of the reciprocal space that can be observed without large distortions is limited to about the second Brillouin zone. The total energy range for quantitative structural analysis can thus be limited, but this can be offset by the ability to measure beams that would be domain-averaged in a regular diffractometer, such as from a 1×2 reconstruction or an hcp substrate [69]. Even under optimum conditions residual distortions in the optics prevent measuring spot positions with accuracies better than a few percent of the first Brilluoin zone, inferior to a dedicated SPA-LEED instrument. The transmission of electrons through the system might be different from a standard LEED diffractometer, although the common usage of the Pendry R factor in structural calculations ameliorates this problem.

The observation of LEED patterns in LEEM started with the first successful instruments [2]. But surprisingly there are only a few studies that have used "traditional" LEED IV calculations coupled to LEED IV measurements in LEEM, as presented in Fig. 18.12 for Cr/W(110) [123]. Both in clean substrates [69] and thin

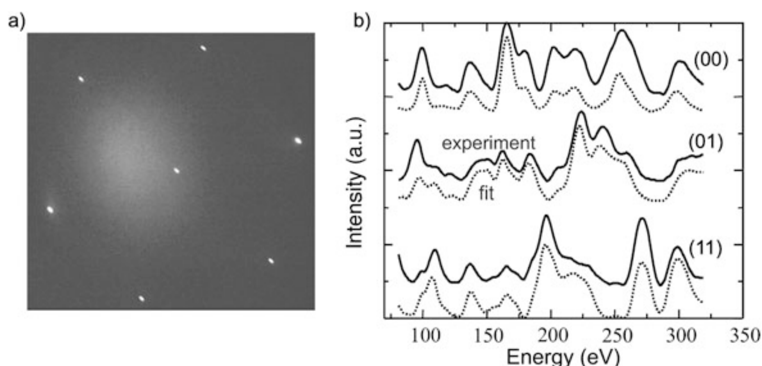

Fig. 18.12 (**a**) LEED pattern of W(110). (**b**) LEED IV measured in LEEM, and multiple scattering fit of the same W(110) surface, reproduced with permission from [123]

films [68, 97], an advantage is the ability to acquire the LEED IV from a single terrace of the substrate or film removing any possible effect of steps, which are not usually included in the multiple scattering calculations. Other than metal surfaces, to date an oxygen reconstruction on Ag [165] has been solved.

In a SPLEEM system, spin-polarized LEED can be measured. Nevertheless, to our knowledge no experimental dataset of SP-LEED has been measured in LEEM.

VLEED In VLEED (0–50 eV) the Ewald sphere is so small that usually only the specular beam or closely-spaced satellites are present. The mean free path can be quite large, extending through films tens of layers thick, and the effect of the band structure on the electron reflectivity cannot be disregarded. The traditional multiple-scattering LEED codes can fail due to convergence limitations, and also due to an incorrect treatment of the dependence of the inner potential with energy. One advantage is that the wavelength of the electrons changes more rapidly at low energies, so the information content is very high.

Besides measuring VLEED in the diffraction mode, where typically only the specular beam is observed, real-space imaging can be used instead. This gives a method to measure the diffraction information of the specular beam with nanometer resolution. This approach has been termed LEEM IV to highlight that the zeroth-order diffraction information is acquired from real-space images. The surface alloy formation of Pd on Cu(100) has been explored in this way [166, 167] by a pixel-by-pixel fitting of the VLEED IV curves to a multiple scattering calculation. The spatially resolved structure gave detailed information about alloy formation around steps. In the same way, monolayers and bilayers of graphene on Ru(0001) have been distinguished [102].

More traditional VLEED determinations can be performed by comparing the experimental data to a calculated unoccupied band structure, including the effect of anisotropic scattering. In this case, the available theoretical calculations [168–170] lag considerably behind the experimental data available. VLEED can be performed with spin-polarized electrons in an SPLEEM, from which information about the

spin-split band structure can be obtained. This was first performed on Co/W(110) [171].

In some cases, comparison of VLEED information with other techniques is possible [172]. As a fingerprinting technique using reference spectra, VLEED has sometimes been used to follow the distribution and evolution of several adsorbates on surfaces, such as carbon monoxide, hydrogen or oxygen [173, 174].

The most popular use of VLEED, though, is the measurement of quantum interference peaks (QIP) in flat films. As mentioned above, the electrons reflected at the film interface and at the film surface interfere, giving rise to maxima and minima of the reflected intensity. The Reflectivity then oscillates as the wavelength of the electrons or the film thickness is changed. Although QIPs are observable at higher energies, the mean free path is then smaller so the QIPs are vanishingly small above 50 eV. A requirement for the observation of QIPs is an abrupt buried interface with high reflectivity. The high reflectivity can arise from a symmetry gap in the substrate electronic structure or a large potential step between film and substrate.

QIPs in VLEED are routinely employed to characterize thickness in ultra-thin films. QIPs have been observed on many different combinations of metal films and substrates [66, 67, 93, 94, 122, 128, 131, 171, 175–179]. It has also been observed in metal/semiconductor combinations [125] and oxide/metal [180] systems.

The QIPs can also be fit to multiple scattering calculations to obtain interplanar spacings in a similar way to regular LEED calculations [175, 177]. Another use of QIPs is determining a material's bulk band structure. The phase accumulation model (PAM, [181, 182]), used to interpret oscillations in the intensity of the photoelectrons emitted from thin films, is also applicable to QIPs. PAM indicates that a continuous electron band in the bulk is reduced to a series of discrete quantum well resonances in a thin film along the direction perpendicular to the interface, with the number of states related to the number of layers. The resonances correspond to conditions of constructive interference for electrons with a given wavelength, taking into account the phase change ϕ of the electron upon reflection at the film/substrate interface and at the film surface:

$$2kd_{film} + \phi = 2n\pi$$

where k is the electron wave vector, d_{film} is the film thickness and n is an integer. As the phase accumulation only depends on the energy, i.e., $\phi(E)$, measuring the thickness d_{osc} between reflectivity maxima at a given energy provides the electron wave vector as $k = \frac{\pi}{d_{osc}}$, allowing a parameter-free measurement of the dispersion of the unoccupied electron band. A limitation of the method is that it assumes that the electronic structure of the thin film is the same (except for the quantization of the levels) as for the bulk material. If the film is strained the assumption will not hold. Also the first few layers are expected to have a different electronic structure due to interactions with the substrate. Bulk structure determinations have been made in this way for Ag [on W(110) and on Fe(100)] [94, 177] and Cu [on Co(100)] [179].

Using a SPLEEM, the spin-dependent electron reflectivity of buried non-magnetic/magnetic interfaces can be studied. From the applied point of view, the study of spin-dependent reflectivity has suggested the design of novel spin-analyzers

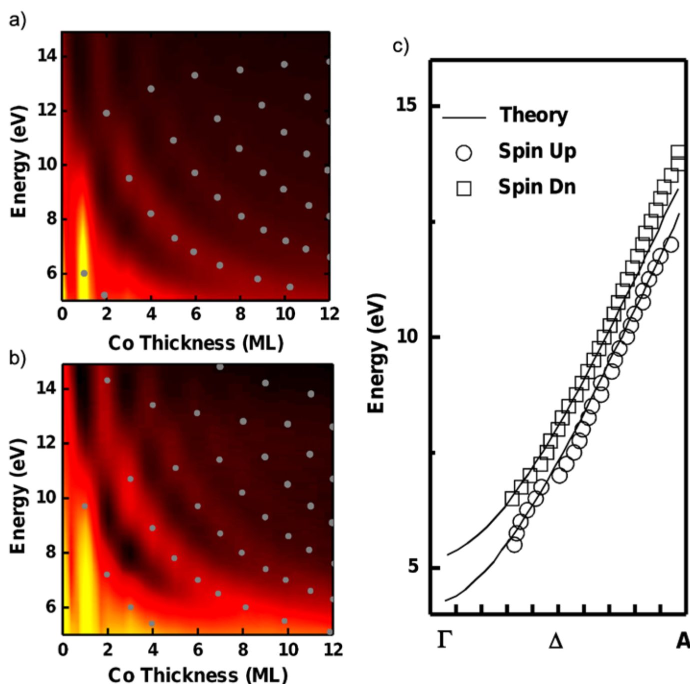

Fig. 18.13 Determining the spin-resolved unoccupied band structure, reprinted with permission from [27]. Electron reflectivity for (**a**) spin-down electrons and (**b**) spin-up electrons shows layer resolved quantum interference peaks. (**c**) Spin-split energy bands retrieved from the quantum interference peaks

[183]. The spin-dependent reflectivity of buried interfaces has been measured in MgO/Fe [180] and Cu/Co(100) [179]. The unoccupied bulk band structure has been measured for Fe [on W(110)] [178] and Co [on Mo(110)] [27] (shown in Fig. 18.13).

18.4.5 Advantages and Limitations vs Other Surface Imaging Techniques

In this section we briefly compare and contrast LEEM to other experimental techniques. The scanning probe microscopies of STM and AFM can routinely achieve atomic resolution, unlike LEEM. However, LEEM has decided advantages in imaging speed and the ease of imaging while changing the surface's state by varying, for example, temperature. X-ray magnetic circular dichroism using PEEM, XMCD-PEEM, characterizes magnetism with elemental specificity, unlike SPLEEM. But the latter technique can perform 3D magnetometry and typically is faster. Surface magneto-optic Kerr effect microscopy, SMOKE, can be performed with applied magnetic fields, unlike SPLEEM. But SPLEEM has much better resolution.

Finally the lateral resolution of scanning electron microscopy (SEM) is comparable to LEEM. But standard SEM is not very sensitive to the surface. For example, single atomic steps are difficult to detect by secondary electrons [184]. However SEM with an immersion lens can give enhanced surface sensitivity [185]. The impact of this technique is still to be determined.

In summary, LEEM is not usually the best technique to make any single type of measurement. But LEEM is capable of many different types of surface analysis, all within one instrument. Also the ability for fast real-spacing imaging combined with selected-area diffraction, is unsurpassed. But the real differentiating capability is making observations in real-time while the surface is evolving. Watching a process occur is incredibly powerful and has revealed many unexpected pathways of surface evolution. Real-time microscopy frequently determines pathways without ambiguity. In contrast, forensic analysis only sees the end result, not the path.

18.5 Future Developments

Two trends in surface science are clear. First, the emphasis on studying increasingly complicated materials. The goal is analyzing the actual "functional" materials used in real applications. Second, characterizing materials under conditions similar to those experienced during their technological use. That is, in the presence of fluids, electric fields and at low and high temperatures, etc. Instrumentation development already in progress and envisioned will allow LEEM to participate fully in these two trends. For example, new schemes of sample cooling will allow the study of materials such as high-temperature superconductors in their superconducting state. New LEEM designs will also be able to operate at much higher pressures. Achieving the same pressures (several millibar) as in near-ambient pressure X-ray photoelectron spectroscopy [186] has technical challenges. However, even at lower pressures, "near-ambient pressure" LEEM/PEEM will be a valuable microscopic compliment to XPS. LEEM-based techniques will increasingly use the spectromicroscopies enabled by imaging energy filters. Electron energy loss and Auger spectromicroscopies need only an electron source. Improved laboratory-based light sources, including focused discharge lamps and ultraviolet lasers, will bring the power of photoemission spectromicroscopy to laboratory studies.

Acknowledgements JdlF acknowledges support from the Spanish Ministry of Science and Innovation through Project No. MAT2009-14578-C03. KFM acknowledges support from the Office of Basic Energy Sciences, Division of Materials Sciences and Engineering of the US DOE under Contract No. DE-AC04-94AL85000.

References

1. L. Veneklasen, Rev. Sci. Instrum. **63**, 5513 (1992)
2. E. Bauer, Rep. Prog. Phys. **57**, 895 (1994)

3. E. Bauer, Surf. Rev. Lett. **5**(6), 1275 (1998)
4. R. Tromp, IBM J. Res. Dev. **44**(4), 503 (2000)
5. R. Phaneuf, A. Schmid, Phys. Today **56**, 50 (2003)
6. N. Rougemaille, A. Schmid, Eur. Phys. J. Appl. Phys. **50**, 20101 (2010)
7. M.S. Altman, J. Phys. Condens. Matter **22**, 084017 (2010)
8. D.B. Williams, C.B. Carter, *Transmission Electron Microscopy: A Textbook for Materials Science*, 2nd edn. (Springer, Berlin, 2009)
9. R.M. Tromp, F.M. Ross, Annu. Rev. Mater. Sci. **30**, 431 (2000)
10. T. Herranz, K. McCarty, B. Santos, M. Monti, J. de la Figuera, Chem. Mater. **22**, 1291 (2010)
11. F. El Gabaly, W. Ling, K. McCarty, J. de la Figuera, Science **308**, 1303 (2005)
12. T. Schmidt, S. Heun, J. Slezak, J. Diaz, K. Prince, G. Lilienkamp, E. Bauer, Surf. Rev. Lett. **5**, 1287 (1998)
13. E. Bauer, Surf. Sci. **299–300**, 102 (1994)
14. W. Telieps, E. Bauer, Ultramicroscopy **17**, 57 (1985)
15. K. Grzelakowski, T. Duden, E. Bauer, H. Poppa, S. Chiang, IEEE Trans. Magn. **30**, 4500 (1994)
16. Elmitec Elektronenmikroskopie GmbH
17. R. Fink, M. Weiss, E. Umbach, D. Preikszas, H. Rose, R. Spehr, P. Hartel, W. Engel, R. Degenhardt, R. Wichtendahl, H. Kuhlenbeck, W. Erlebach, K. Ihmann, R. Schlogl, H. Freund, A. Bradshaw, G. Lilienkamp, T. Schmidt, E. Bauer, G. Benner, J. Electron Spectrosc. Relat. Phenom. **84**, 231 (1997)
18. R. Tromp, J. Hannon, A. Ellis, W. Wan, A. Berghaus, O. Schaff, Ultramicroscopy **110**, 852 (2010)
19. Specs Surface Nanoanalysis Gmbh
20. M. Van Hove, S. Tong, *Surface Crystallography by LEED* (Springer, Berlin, 1979)
21. L.J. Clarke, *Surface Crystallography: An Introduction to Low Energy Electron Diffraction* (Wiley, New York, 1985)
22. S. Nepijko, N. Sedov, Adv. Imaging Electron Phys. **102**, 273 (1998)
23. S.M. Kennedy, C.X. Zheng, W.X. Tang, D.M. Paganin, D.E. Jesson, Proc. R. Soc. A **466**, 2857 (2010)
24. J. de la Figuera, N. Bartelt, K. McCarty, Surf. Sci. **600**, 4062 (2006)
25. T. Herranz, B. Santos, K. McCarty, J. de la Figuera, Surf. Sci. **605**, 903 (2011)
26. A.B. Pang, T. Müller, M. Altman, E. Bauer, J. Phys. Condens. Matter **21**(31), 314006 (2009)
27. J.S. Park, A. Quesada, Y. Meng, J. Li, E. Jin, H. Son, A. Tan, J. Wu, C. Hwang, H.W. Zhao, A.K. Schmid, Z.Q. Qiu, Phys. Rev. B **83**, 113405 (2011)
28. J. Pendry, *Low Energy Electron Diffraction: The Theory and Its Application to Determination of Surface Structure* (Academic Press, San Diego, 1974)
29. W. Chung, M. Altman, Ultramicroscopy **74**, 237 (1998)
30. S. Kennedy, N. Schofield, D. Paganin, D. Jesson, Surf. Rev. Lett. **16**, 855 (2009)
31. T. Schmidt, H. Marchetto, P. Levesque, U. Groh, F. Maier, D. Preikszas, P. Hartel, R. Spehr, G. Lilienkamp, W. Engel, R. Fink, E. Bauer, H. Rose, E. Umbach, H. Freund, Ultramicroscopy **110**, 1358 (2010)
32. K.N. Maffitt, Rev. Sci. Instrum. **39**, 259 (1968)
33. M. Mankos, D. Adler, L. Veneklasen, E. Munro, Phys. Proc. **1**, 485 (2008)
34. E. Bauer, in *Modern Techniques for Characterizing Magnetic Materials*, ed. by Y. Zhu (Springer, Berlin, 2005), pp. 361–382
35. E. Bauer, in *Magnetic Microscopy of Nanostructures*, ed. by H. Hopster, H.P. Oepen (Springer, Berlin, 2005), pp. 111–136
36. P.W. Palmberg, R.E. DeWames, L.A. Vredevoe, Phys. Rev. Lett. **21**, 682 (1968)
37. K.S.R. Menon, S. Mandal, J. Das, T.O. Mentes, M.A. Niño, A. Locatelli, R. Belkhou, Phys. Rev. B **84**, 132402 (2011). doi:10.1103/PhysRevB.84.132402
38. G. Rempfer, D. Desloge, W. Skoczylas, O. Griffith, Microsc. Microanal. **3**, 14 (1997)
39. R. Tromp, Ultramicroscopy **111**, 273 (2011)
40. K. Tsuno, T. Yasue, T. Koshikawa, Appl. Surf. Sci. **256**, 1035 (2009)

41. R. Tromp, Y. Fujikawa, J. Hannon, A. Ellis, A. Berghaus, O. Schaff, J. Phys. Condens. Matter **21**(31), 314007 (2009)
42. K. Grzelakowski, E. Bauer, Rev. Sci. Instrum. **67**, 742 (1996)
43. P. Grivet, *Electron Optics*, revised edn. (Pergamon, Elmsford, 1965)
44. G.F. Rempfer, J. Appl. Phys. **57**, 2385 (1985)
45. P. Adamec, E. Bauer, B. Lencova, Rev. Sci. Instrum. **69**, 3583 (1998)
46. Kimball Physics, Inc, Tech. Bull. (1991)
47. D.T. Pierce, R.J. Celotta, G. Wang, W.N. Unertl, A. Galejs, C.E. Kuyatt, S.R. Mielczarek, Rev. Sci. Instrum. **51**, 478 (1980)
48. X. Jin, N. Yamamoto, Y. Nakagawa, A. Mano, T. Kato, M. Tanioku, T. Ujihara, Y. Takeda, S. Okumi, M. Yamamoto, T. Nakanishi, T. Saka, H. Horinaka, T. Kato, T. Yasue, T. Koshikawa, Appl. Phys. Express **1**, 045002 (2008)
49. T. Duden, E. Bauer, Rev. Sci. Instrum. **66**, 2861 (1995)
50. J. Chmelik, L. Veneklasen, G. Marx, Optik **83**(5), 155 (1989)
51. V. Kolarik, M. Mankos, L. Veneklasen, Optik **87**, 1 (1991)
52. W. Wan, J. Feng, H. Padmore, Nucl. Instrum. Methods Phys. Res. **564**, 537 (2006)
53. R. van Gastel, I. Sikharulidze, S. Schramm, J. Abrahams, B. Poelsema, R. Tromp, S. van der Molen, Ultramicroscopy **110**, 33 (2009)
54. L. Veneklasen, Ultramicroscopy **36**, 76 (1991)
55. Y. Fujikawa, T. Sakurai, R.M. Tromp, Phys. Rev. Lett. **100**, 126803 (2008)
56. J. Sun, J.B. Hannon, R.M. Tromp, P. Johari, A.A. Bol, V.B. Shenoy, K. Pohl, ACS Nano **4**, 7073 (2010)
57. Y. Fujikawa, T. Sakurai, R.M. Tromp, Phys. Rev. B **79**, 121401 (2009)
58. K. McCarty, N. Bartelt, Surf. Sci. **540**, 157 (2003)
59. K. McCarty, N. Bartelt, Surf. Sci. **527**, L203 (2003)
60. K. McCarty, N. Bartelt, Phys. Rev. Lett. **90**, 046104 (2003)
61. S. Kodambaka, N. Israeli, J. Bareño, W. Swiech, K. Ohmori, I. Petrov, J.E. Greene, Surf. Sci. **560**, 53 (2004)
62. S. Kodambaka, S. Khare, W. Swiech, K. Ohmori, I. Petrov, J. Greene, Nature **429**, 49 (2004)
63. S. Kodambaka, J. Bareno, S. Khare, W. Swieach, I. Petrov, J. Greene, J. Appl. Phys. **98**, 034901 (2005)
64. B. Unal, Y. Sato, K. McCarty, N. Bartelt, T. Duden, C. Jenks, A. Schmid, P. Thiel, J. Vac. Sci. Technol. A **27**, 1249 (2009)
65. Y. Sato, B. Unal, T. Lograsso, P. Thiel, A. Schmid, T. Duden, N. Bartelt, K. McCarty, Phys. Rev. B **81**, 161406(R) (2010)
66. K. McCarty, Nano Lett. **6**, 858 (2006)
67. W. Ling, N. Bartelt, K. McCarty, C. Carter, Phys. Rev. Lett. **95**, 166105 (2005)
68. F. El Gabaly, J. Puerta, C. Klein, A. Saa, A. Schmid, K. McCarty, J. Cerda, J. de la Figuera, New J. Phys. **9**, 80 (2007)
69. J. de la Figuera, J. Puerta, J. Cerda, F. El Gabaly, K. McCarty, Surf. Sci. **600**, L105 (2006)
70. J. Maxson, N. Perkins, D. Savage, A. Woll, L. Zhang, T. Kuech, M. Lagally, Surf. Sci. **464**, 217 (2000)
71. N. Bartelt, W. Theis, R. Tromp, Phys. Rev. B **54**, 11741 (1996)
72. M. Mundshau, E. Bauer, W. Telieps, W. Swiech, Surf. Sci. **223**, 413 (1989)
73. N. Bartelt, R. Tromp, E. Williams, Phys. Rev. Lett. **73**, 1656 (1994)
74. M. Ondrejcek, W. Swiech, M. Rajappan, C. Flynn, Phys. Rev. B **72**, 085422 (2005)
75. M. Ondrejcek, M. Rajappan, W. Swiech, C. Flynn, Surf. Sci. **574**, 111 (2005)
76. S. Kodambaka, S. Khare, I. Petrov, J. Greene, Surf. Sci. Rep. **60**, 55 (2006)
77. B. Poelsema, J.B. Hannon, N.C. Bartelt, G.L. Kellogg, Appl. Phys. Lett. **84**, 2551 (2004)
78. K. McCarty, J. Nobel, N. Bartelt, Nature **412**, 622 (2001)
79. G. Kellogg, N. Bartelt, Surf. Sci. **577**, 151 (2005)
80. W. Ling, N. Bartelt, K. Pohl, J. de la Figuera, R. Hwang, K. McCarty, Phys. Rev. Lett. **93**, 166101 (2004)

81. M. Ondrejcek, W. Swiech, I. Petrov, M. Rajappan, C.P. Flynn, Microsc. Res. Tech. **72**, 197 (2009)
82. W. Swiech, M. Ondrejcek, C. Flynn, J. Phys. Condens. Matter **21**, 314021 (2009)
83. R.M. Tromp, M. Mankos, Phys. Rev. Lett. **81**, 1050 (1998)
84. E. Loginova, N. Bartelt, P. Feibelman, K. McCarty, New J. Phys. **10**, 093026 (2008)
85. J. Hannon, R. Tromp, Annu. Rev. Mater. Res. **33**, 263 (2003)
86. W. Telieps, E. Bauer, Surf. Sci. **162**, 163 (1985)
87. J. Hannon, H. Hibino, N. Bartelt, B. Swartzentruber, T. Ogino, G. Kellogg, Nature **405**, 552 (2000)
88. J. Hannon, F. Heringdorf, J. Tersoff, R. Tromp, Phys. Rev. Lett. **86**, 4871 (2001)
89. H. Hibino, Y. Watanabe, C. Hu, I.S.T. Tsong, Phys. Rev. B **72**, 245424 (2005)
90. J. Maxson, D. Savage, F. Liu, R. Tromp, M. Reuter, M. Lagally, Phys. Rev. Lett. **85**, 2152 (2000)
91. R. Tromp, W. Theis, N. Bartelt, Phys. Rev. Lett. **77**, 2522 (1996)
92. Y. Sato, S. Chiang, Surf. Sci. **603**, 2300 (2009)
93. M. Mundschau, E. Bauer, W. Swiech, J. Appl. Phys. **65**, 581 (1989)
94. K. Man, Z. Qiu, M. Altman, Phys. Rev. Lett. **93**, 236104 (2004)
95. K. Man, Q. Guo, M. Altman, Surf. Sci. **600**, 1060 (2006)
96. N. Rougemaille, F. El Gabaly, R. Stumpf, A. Schmid, K. Thürmer, N. Bartelt, J. de la Figuera, Phys. Rev. Lett. **99**, 106101 (2007)
97. B. Santos, J. Puerta, J. Cerda, T. Herranz, K. McCarty, J. de la Figuera, New J. Phys. **12**, 023023 (2010)
98. K. Man, M. Tringides, M. Loy, M. Altman, Phys. Rev. Lett. **101**, 226102 (2008)
99. T. Schmidt, E. Bauer, Phys. Rev. B **62**, 15815 (2000)
100. J. Hannon, J. Tersoff, M. Reuter, R. Tromp, Phys. Rev. Lett. **89**, 266103 (2002)
101. R. Tromp, J. Hannon, Surf. Rev. Lett. **9**, 1565 (2002)
102. P.W. Sutter, J. Flege, E.A. Sutter, Nat. Mater. **7**, 406 (2008)
103. E. Loginova, S. Nie, K. Thurmer, N. Bartelt, K. McCarty, Phys. Rev. B **80**, 085430 (2009)
104. E. Loginova, N. Bartelt, P. Feibelman, K. McCarty, New J. Phys. **11**, 063046 (2009)
105. E. Starodub, S. Maier, I. Stass, N. Bartelt, P. Feibelman, M. Salmeron, K. McCarty, Phys. Rev. B **80**, 235422 (2009)
106. K. McCarty, P. Feibelman, E. Loginova, N. Bartelt, Carbon **47**, 1806 (2009)
107. Y. Murata, E. Starodub, B. Kappes, C. Ciobanu, N. Bartelt, K. McCarty, S. Kodambaka, Appl. Phys. Lett. **97**, 143114 (2010)
108. E. Starodub, N. Bartelt, K. McCarty, J. Phys. Chem. C **114**, 5134 (2010)
109. J. Wofford, S. Nie, K. McCarty, N. Bartelt, O. Dubon, Nano Lett. **10**, 4890 (2010)
110. S. Nie, A. Walter, N. Bartelt, E. Starodub, A. Bostwick, E. Rotenberg, K. McCarty, ACS Nano **5**, 2298 (2011)
111. T. Ohta, F.E. Gabaly, A. Bostwick, J.L. McChesney, K.V. Emtsev, A.K. Schmid, T. Seyller, K. Horn, E. Rotenberg, New J. Phys. **10**, 023034 (2008)
112. R. Tromp, J. Hannon, Phys. Rev. Lett. **102**, 106104 (2009)
113. D. Siegel, S. Zhou, F.E. Gabaly, A. Schmid, K. McCarty, A. Lanzara, Phys. Rev. B **80**, 241407(R) (2009)
114. K. McCarty, Surf. Sci. **543**, 185 (2003)
115. K. McCarty, N. Bartelt, J. Cryst. Growth **270**, 691 (2004)
116. J. Pierce, K. McCarty, Phys. Rev. B **71**, 125428 (2005)
117. K. McCarty, J. Pierce, C. Carter, Appl. Phys. Lett. **88**, 141902 (2006)
118. J. Pierce, N. Bartelt, R. Stumpf, K. McCarty, Phys. Rev. B **77**, 195438 (2008)
119. J. Flege, J. Hrbek, P. Sutter, Phys. Rev. B **78**, 165407 (2008)
120. B. Santos, E. Loginova, A. Mascaraque, A. Schmid, K. McCarty, J. de la Figuera, J. Phys. Condens. Matter **21**, 314011 (2009)
121. J.B. Hannon, Science **313**, 1266 (2006)
122. W. Ling, J. Hamilton, K. Thurmer, G. Thayer, J. de la Figuera, R. Hwang, C. Carter, N. Bartelt, K. McCarty, Surf. Sci. **600**, 1735 (2006)

123. B. Santos, J. Puerta, J. Cerda, R. Stumpf, K. von Bergmann, R. Wiesendanger, M. Bode, K. McCarty, J. de la Figuera, New J. Phys. **10**, 013005 (2008)
124. F. El Gabaly, S. Gallego, M.C. Muñoz, L. Szunyogh, P. Weinberger, C. Klein, A. Schmid, K. McCarty, J. de la Figuera, Phys. Rev. Lett. **96**, 147202 (2006)
125. R. Tromp, A. Vandergon, F. Legoues, M. Reuter, Phys. Rev. Lett. **71**, 3299 (1993)
126. S. Tang, S. Kodambaka, W. Swiech, I. Petrov, C. Flynn, T. Chiang, Phys. Rev. Lett. **96**, 126106 (2006)
127. K. McCarty, J. Hamilton, Y. Sato, A. Saa, R. Stumpf, J. de la Figuera, K. Thürmer, F. Jones, A. Schmid, A. Talin, N. Bartelt, New J. Phys. **11**, 043001 (2009)
128. W. Ling, T. Giessel, K. Thürmer, R. Hwang, N. Bartelt, K. McCarty, Surf. Sci. **570**, L297 (2004)
129. F.E. Gabaly, A.K. Schmid, Method for preparing ultraflat, atomically perfect areas on large regions of a crystal surface by heteroepitaxy deposition, 2009
130. F.E. Gabaly, N.C. Bartelt, A.K. Schmid, J. Phys. Condens. Matter **21**, 314019 (2009)
131. L. Aballe, A. Barinov, A. Locatelli, T. Mentes, M. Kiskinova, Phys. Rev. B **75**, 115411 (2007)
132. A. Locatelli, L. Aballe, T. Mentes, F. Guo, M. Kiskinova, Surf. Sci. **601**, 4663 (2007)
133. J. de la Figuera, F. Leonard, N. Bartelt, R. Stumpf, K. McCarty, Phys. Rev. Lett. **100**, 186102 (2008)
134. T.O. Mentes, A. Locatelli, L. Aballe, E. Bauer, Phys. Rev. Lett. **101**, 085701 (2008)
135. J. Hannon, J. Tersoff, R. Tromp, Science **295**, 299 (2002)
136. G. Thayer, J. Hannon, R. Tromp, Nat. Mater. **3**, 95 (2004)
137. N. Medhekar, V. Shenoy, J. Hannon, R. Tromp, Phys. Rev. Lett. **99**, 156102 (2007)
138. R. Plass, J. Last, N. Bartelt, G. Kellogg, Nature **412**, 875 (2001)
139. R. Plass, N. Bartelt, G. Kellogg, J. Phys. Condens. Matter **14**, 4227 (2002)
140. R. van Gastel, R. Plass, N. Bartelt, G. Kellogg, Phys. Rev. Lett. **91**, 055503 (2003)
141. R. van Gastel, N. Bartelt, P. Feibelman, F. Leonard, G. Kellogg, Phys. Rev. B **70**, 245413 (2004)
142. R. van Gastel, N. Bartelt, G. Kellogg, Phys. Rev. Lett. **96**, 036106 (2006)
143. K. McCarty, J. Nobel, N. Bartelt, Phys. Rev. B **71**, 085421 (2005)
144. P. Hou, K. McCarty, Scr. Mater. **54**, 937 (2006)
145. D. Wu, W.K. Lau, Z.Q. He, Y.J. Feng, M.S. Altman, C.T. Chan, Phys. Rev. B **62**, 8366 (2000)
146. K. Man, Y. Feng, M. Altman, Phys. Rev. B **74**, 085420 (2006)
147. K. Man, Y. Feng, C. Chan, M. Altman, Surf. Sci. **601**, L95 (2007)
148. A.K. Schmid, N.C. Bartelt, R.Q. Hwang, Science **290**, 1561 (2000)
149. T. Duden, E. Bauer, Phys. Rev. Lett. **77**, 2308 (1996)
150. E. Bauer, T. Duden, R. Zdyb, J. Phys. D **35**, 2327 (2002)
151. K. Man, R. Zdyb, S. Huang, T. Leung, C. Chan, E. Bauer, M. Altman, Phys. Rev. B **67**, 184402 (2003)
152. R. Zdyb, E. Bauer, Phys. Rev. B **67**, 134420 (2003)
153. R. Zdyb, A. Locatelli, S. Heun, S. Cherifi, R. Belkhou, E. Bauer, Surf. Interface Anal. **37**, 239 (2005)
154. E. Bauer, R. Belkhou, S. Cherifi, R. Hertel, S. Heun, A. Locatelli, A. Pavlovska, R. Zdyb, N. Agarwal, H. Wang, Surf. Interface Anal. **38**, 1622 (2006)
155. H. Ding, A. Schmid, D. Li, K. Guslienko, S. Bader, Phys. Rev. Lett. **94**, 157202 (2005)
156. N. Rougemaille, A. Schmid, J. Appl. Phys. **99**, 08S502 (2006)
157. R. Zdyb, A. Pavlovska, M. Jalochowski, E. Bauer, Surf. Sci. **600**, 1586 (2006)
158. R. Zdyb, E. Bauer, Phys. Rev. Lett. **100**, 155704 (2008)
159. C. Klein, R. Ramchal, M. Farle, A. Schmid, Surf. Interface Anal. **38**, 1550 (2006)
160. T. Duden, E. Bauer, Phys. Rev. B **59**, 468 (1999)
161. C. Klein, R. Ramchal, A. Schmid, M. Farle, Phys. Rev. B **75**, 193405 (2007)
162. F. El Gabaly, K. McCarty, A. Schmid, J. de la Figuera, M.C. Muñoz, L. Szunyogh, P. Weinberger, S. Gallego, New J. Phys. **10**, 073024 (2008)
163. R. Zdyb, T. Mentes, A. Locatelli, M. Nino, E. Bauer, Phys. Rev. B **80**, 184425 (2009)

164. M.H. von Hoegen, Z. Kristallogr. **214**, 591 (1999)
165. R. Reichelt, S. Günther, J. Wintterlin, W. Moritz, L. Aballe, T.O. Mentes, J. Chem. Phys. **127**, 134706 (2007)
166. J. Hannon, J. Sun, K. Pohl, G. Kellogg, Phys. Rev. Lett. **96**, 246103 (2006)
167. J. Sun, J. Hannon, G. Kellogg, K. Pohl, Phys. Rev. B **76**, 205414 (2007)
168. M. Lindroos, H. Pfnür, D. Menzel, Phys. Rev. B **33**, 6684 (1986)
169. M. Lindroos, H. Pfnür, P. Feulner, D. Menzel, Surf. Sci. **180**, 237 (1987)
170. I. Bartos, M.A.V. Hove, M.S. Altman, Surf. Sci. **352–354**, 660 (1996)
171. T. Scheunemann, R. Feder, J. Henk, E. Bauer, T. Duden, H. Pinkvos, H. Poppa, K. Wurm, Solid State Commun. **104**, 787 (1997)
172. R.C. Jaklevic, L.C. Davis, Phys. Rev. B **26**, 5391 (1982)
173. A.K. Schmid, W. Swiech, C.S. Rastomjee, B. Rausenberger, W. Engel, E. Zeitler, A.M. Bradshaw, Surf. Sci. **331–333**, 225 (1995)
174. C.M. Yim, K.L. Man, X. Xiao, M.S. Altman, Phys. Rev. B **78**, 155439 (2008)
175. H. Poon, S. Tong, W. Chung, M. Altman, Surf. Rev. Lett. **5**, 1143 (1998)
176. M. Altman, W. Chung, Z. He, H. Poon, S. Tong, Appl. Surf. Sci. **169–170**, 82 (2001)
177. M.S. Altman, J. Phys. Condens. Matter **17**, S1305 (2005)
178. R. Zdyb, E. Bauer, Phys. Rev. Lett. **88**, 166403 (2002)
179. Y.Z. Wu, A.K. Schmid, M.S. Altman, X.F. Jin, Z.Q. Qiu, Phys. Rev. Lett. **94**, 027201 (2005)
180. Y. Wu, A. Schmid, Z. Qiu, Phys. Rev. Lett. **97**, 217205 (2006)
181. J.E. Ortega, F.J. Himpsel, G.J. Mankey, R.F. Willis, Phys. Rev. B **47**, 1540 (1993)
182. Z.Q. Qiu, N.V. Smith, J. Phys. Condens. Matter **14**, R169 (2002)
183. C. Jozwiak, J. Graf, G. Lebedev, N. Andresen, A. Schmid, A. Fedorov, F. El Gabaly, W. Wan, A. Lanzara, Z. Hussain, Rev. Sci. Instrum. **81**, 053904 (2010)
184. Y. Homma, M. Tomita, T. Hayashi, Ultramicroscopy **52**, 187 (1993)
185. I. Müllerová, K. Matsuda, P. Hrncirík, L. Frank, Surf. Sci. **601**, 4768 (2007)
186. F.F. Tao, M. Salmeron, Science **331**, 171 (2011)